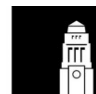

This is a repository copy of *GeSn/SiGeSn Heterostructure and Multi Quantum Well Lasers*.

White Rose Research Online URL for this paper:
http://eprints.whiterose.ac.uk/137759/

Version: Accepted Version

Article:
Stange, D, von den Driesch, N, Zabel, T et al. (12 more authors) (2018) GeSn/SiGeSn Heterostructure and Multi Quantum Well Lasers. ACS Photonics, 5 (11). pp. 4628-4636. ISSN 2330-4022

https://doi.org/10.1021/acsphotonics.8b01116

© 2018 American Chemical Society. This is an author produced version of a paper published in ACS Photonics. Uploaded in accordance with the publisher's self-archiving policy.

Reuse
Items deposited in White Rose Research Online are protected by copyright, with all rights reserved unless indicated otherwise. They may be downloaded and/or printed for private study, or other acts as permitted by national copyright laws. The publisher or other rights holders may allow further reproduction and re-use of the full text version. This is indicated by the licence information on the White Rose Research Online record for the item.

Takedown
If you consider content in White Rose Research Online to be in breach of UK law, please notify us by emailing eprints@whiterose.ac.uk including the URL of the record and the reason for the withdrawal request.

eprints@whiterose.ac.uk
https://eprints.whiterose.ac.uk/

GeSn/SiGeSn Heterostructure and Multi Quantum Well Lasers

Daniela Stange[1*], Nils von den Driesch[1,2], Thomas Zabel[3], Francesco Armand-Pilon[3], Denis Rainko[1], Bahareh Marzban[4], Peter Zaumseil[5], Jean-Michel Hartmann[6], Zoran Ikonic[7], Giovanni Capellini[5,8], Siegfried Mantl[1], Hans Sigg[3], Jeremy Witzens[4], Detlev Grützmacher[1], and Dan Buca[1]

[1]Peter Grünberg Institute (PGI 9) and JARA-Fundamentals of Future Information Technologies, Forschungszentrum Jülich, 52425 Jülich, Germany

[2]JARA-Institute Green IT, RWTH Aachen University, 52075 Aachen, Germany

[3]Laboratory for Micro- and Nanotechnology (LMN), Paul Scherrer Institute, CH-5232 Villigen, Switzerland

[4]Institute of Integrated Photonics and JARA-Fundamentals of Future Information Technologies, RWTH Aachen University, 52074 Aachen, Germany

[5]IHP, Im Technologiepark 25, 15236 Frankfurt (Oder), Germany

[6]Univ. Grenoble Alpes, CEA, LETI, F-38000 Grenoble, France

[7]Pollard Institute, School of Electronic and Electrical Engineering, University of Leeds, Leeds LS2 9JT, United Kingdom

[8]Department of Sciences, Università Roma Tre, 00146 Roma, Italy

*corresponding author email: d.stange@fz-juelich.de | telephone: +492461-614505

GeSn and SiGeSn are promising materials for the fabrication of a group IV laser source offering a number of design options from bulk to heterostructures and quantum wells. Here, we investigate GeSn/SiGeSn multi quantum wells using the optically pumped laser effect. Three complex heterostructures were grown on top of 200 nm thick strain relaxed $Ge_{0.9}Sn_{0.1}$ buffers. The lasing is investigated in terms of threshold and maximal lasing operation temperature by comparing multiple quantum well to double heterostructure samples. Pumping under two different wavelengths of 1064 nm and 1550 nm yield comparable lasing thresholds. The design with multi quantum wells reduces the lasing threshold to (40 ± 5) kW/cm^2 at 20 K, almost 10 times lower than for bulk structures. Moreover, 20 K higher maximal lasing temperatures were found for lower energy pumping of 1550 nm.

Keywords: Group IV Photonics; Heterostructures; Microdisk Cavities; MIR-Lasers; Multi-Quantum-Wells; (Si)GeSn

Increasing demand for intra- and inter-chip data throughput (the so-called I/O bottleneck[1]) requires

modifications to current CMOS technology in order to extend the bandwidth and reduce power consumption. In addition to power-optimized transistors[2,3], the integration of photonic circuits with silicon (Si) electronics features the potential to meet such requirements[4,5]. Laser sources based on III-V materials and heterogeneously integrated on Si show excellent performance. However, compared to monolithic integration based on epitaxial growth, wafer bonding remains a complex technology which is likely to result in increased manufacturing costs. Lasing in III-V materials grown directly on a Si recently underwent substantial progress[6,7], in particular with the demonstration of electrically pumped lasers grown on non-offcut Si substrates. However, the realization of a laser based entirely on Si-like non-polar group IV material system, and thus without any anti-phase domains or contamination issues, could be a powerful enabler for a more ubiquitous implementation of ultra-low cost transceivers at lower architecture levels[8] in high-performance computing systems.

Direct bandgap GeSn semiconductors were first demonstrated in 2015[9], including the operation at cryogenic temperatures of optically pumped Fabry-Perot (FP) waveguide lasers. This function is based on modification of the Ge band structure by Sn incorporation. With increasing Sn concentration, the conduction band at Γ drops faster than at L, turning GeSn at a certain Sn content into a direct bandgap semiconductor. A direct bandgap and lasing were demonstrated already in an unstrained alloy with 8 at.% Sn[10]. Since then, results have been reproduced and improved by other groups, leading to the fabrication of GeSn lasers with Sn concentrations of up to 18 at.% and presently featuring lasing operating temperatures up to 180 K[11–13]. Further development of GeSn lasers sets the main target as: i) increasing the laser operating temperature to room temperature; ii) reducing the laser pumping threshold to values significantly below the few hundreds of kW/cm^2 currently required and iii) fabricating an electrically pumped laser.

One of the most serious problems, that has to be overcome, are material defects that cause non-radiative recombination. For example, the laser material used for the demonstration of optically pumped lasing in GeSn[9] has a misfit dislocation network located at the interface with the Ge strain-relaxed buffer underneath and may also contain point defects in the volume of the material. To address this problem, we focus here on the design and deposition of advanced heterostructures grown on Si (001) wafers, which are based on the combination of direct bandgap GeSn alloys – the active layers – and SiGeSn alloys used as cladding layers (confining potential barriers). A related goal is to separate carriers from the defective interface(s). Quantum wells localize carriers, decrease the active material volume and modify the joint density of states improving the material gain at lower carrier densities than in bulk[14]. Both aspects contribute to a reduction of the lasing threshold. In addition, in a quantum well, Auger recombination is

expected to be suppressed[15], which could become an important feature in view of the usually high Auger coefficients in low bandgap materials[16], like GeSn and will be of particular importance as the lasing temperature is increased.

Previous studies of multi quantum well (MQW) stacks with indirect bandgap GeSn active layers have shown that Ge is not an appropriate barrier material, in particular for the confinement of electrons[17]. Instead, employing SiGeSn ternary alloys enables confinement of electrons and holes simultaneously, as demonstrated by an improved emission efficiency at low temperatures of light emitting diodes (LED) grown in an MQW design[18,19].

In this letter we investigate the lasing properties of microdisk cavities fabricated from GeSn- MQW heterostructures with SiGeSn barriers. The Sn concentration in the active layers was chosen moderately high (~13 at.%). The strain relaxed GeSn buffer layer sandwiched between the Ge virtual substrate (VS) and the heterostructure is intended to keep the misfit dislocations at the Ge-VS interface, distant from the active material. Our study comprises the investigation of MQW lasers with different well thicknesses, and a comparison with a double heterostructure (DHS) in terms of lasing threshold, emitted light intensity and band structure.

RESULTS AND DISCUSSION

As-grown Layers

The growth details and structural characterization of the DHS and MQW laser stacks discussed here, are given in reference [20], and the main parameters are summarized in Table 1. In the DHS design, although the compressive strain is partly relaxed via the $Ge_{0.9}Sn_{0.1}$ buffer underneath, the thick GeSn active layer with a higher Sn content builds up a large strain energy. This results in the formation of a second misfit dislocation network between the bottom $Si_{0.055}Ge_{0.83}Sn_{0.115}$ cladding and the $Ge_{0.855}Sn_{0.145}$ active layer (see Figure S1). This second misfit dislocation network is particularly undesirable, since it is in the immediate vicinity of the gain material where carriers accumulate. This reduces the role of large energy band offset of the bottom SiGeSn cladding layer, which is not able to separate misfit dislocations from the active layers. The DHS laser thus shows similar characteristics as the bulk GeSn laser.

Structure Name	Sn content in active layer/QW (at.%)	thickness of active layer/QW (nm)	Si/Sn content in top cladding (at.%)	Si/Sn content in bottom cladding (at.%)	Si/Sn content in barrier (at.%)	barrier thickness (nm)
DHS	14.5	380	4.5/14.0	5.5/11.5	-	-

MQW-A	13.3	22·(10x)	-	-	4.8/13.0	22
MQW-B	13.5	12·(10x)	-	-	5.2/13.4	16

Table 1: Alloy compositions and layer thicknesses of the investigated heterostructures, measured by atom probe tomography (MQW-A) and energy dispersive X-ray spectroscopy (DHS and MQW-B).

One way to eliminate the misfit dislocation network formation is the epitaxial growth of strain compensating SiGeSn/GeSn wells. Two MQWs with 10 periods of {$Si_{0.05}Ge_{0.82}Sn_{0.13}$/$Ge_{0.87}Sn_{0.13}$} were grown on the same buffer as the DHS. All quantum wells have identical compositions and layer thicknesses throughout the MQW stacks. Well and barrier thicknesses are respectively 22 nm/22 nm for MQW-A and 12 nm/16 nm for MQW-B. A line scan of an energy dispersive X-ray spectroscopy analysis of MQW-A is exemplarily displayed in Figure 1a. In contrast to the DHS structure, no misfit dislocations are visible at the interface between the relaxed GeSn buffer and the MQW layers, indicating pseudomorphic growth of the MQW on top of the GeSn buffer, cf. Figure 1b. This important feature is confirmed by the X-ray diffraction reciprocal space mapping (XRD-RSM) in Figure 1c. Here, XRD of the (-2-24) reflex was measured and the numbers in the figure are assigned to satellite peaks of different orders from the GeSn/SiGeSn superlattice. It should be noted, that in the MQW structures the Sn/Si content, and therefore also the strain in the active $Ge_{0.87}Sn_{0.13}$ wells (-0.68%) and in $Si_{0.05}Ge_{0.82}Sn_{0.13}$ barriers (-0.43%), are different. This results in a reduction of the averaged elastic strain in the stack compared to DHS. It allows a considerable increase of the total stack thickness without any additional plastic relaxation. And particularly, the carriers in the MQWs are separated by the SiGeSn barriers from the misfit dislocations located at the Ge-VS/$Ge_{0.9}Sn_{0.1}$ interface.

From the model of People and Bean[21], the critical thickness of a similar MQW stack grown on top of a GeSn buffer is calculated to be 269 nm, exceeding the total stack thickness of MQW-A. However, for the individual layers, SiGeSn barrier and GeSn well, the critical thickness amounts to 400 nm and 176 nm, respectively, which is below the grown thicknesses of each layer. Therefore MQW-A is anticipated to be metastable. The total thickness of MQW-B of ~270 nm is indeed in the range of the critical thickness of the total stack.

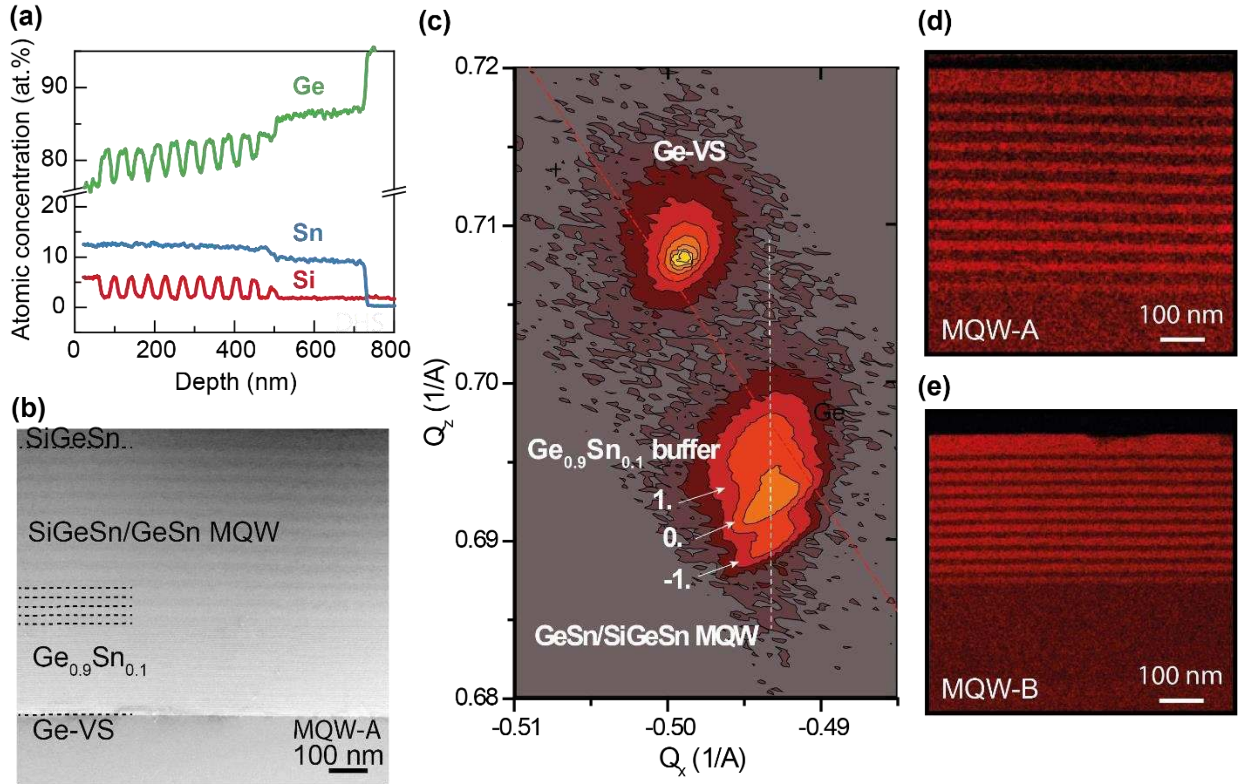

Figure 1 Structural characterization of DHS and MQW stacks. **(a)** EDX line scan of the MQW shows the content of Si, Ge and Sn throughout the heterostructure. **(b)** X-TEM of MQW-A reveals an absence of dislocations between the GeSn buffer and the MQW region. **(c)** XRD-RSM proving the coherent growth of GeSn/SiGeSn quantum wells. The EDX elemental Si maps from **(d)** MQW-A and **(e)** MQW-B at the same magnification show the regularity of the stacks and also illustrate the difference in layer thicknesses.

The different well/barrier thicknesses between MQW-A and MQW-B are evidenced by the Si signals of energy dispersive X-ray spectra (EDX) shown in Figures 1d and 1e: wells and barriers are regularly spaced, with Si content varying between 0 and 5 at.%.

The effective bandgap values, given in Table 2, correspond to the energy differences between the first quantized levels of heavy holes (HH) and Γ-valley electrons in the actual structure. The calculations include residual strain and also quantization effects. The quantum state energies are inversely proportional to the effective masses of the conduction and valence bands. This affects the directness of the material (defined as $\Delta E_{L-\Gamma}=E_L-E_\Gamma$), which is considerably reduced in thinner wells since the electron effective mass at Γ (m^*_Γ[100]= 0.031m_e) is ~2.7 times smaller than at L (m^*_L= 0.117m_e)[22]. We define the effective well-barrier energy offsets for electrons, cf. Table 2, as the energy difference between the lowest quantized Γ-valley state of the GeSn wells and the Γ-valley/L-valley energy of the SiGeSn cladding, respectively. The

confinement for holes is weaker than for electrons and the barrier height here is between 56 meV and 24 meV.

Structure Name	Bandgap E_g (meV)	Directness $\Delta E_{L-\Gamma}$ (meV)	Offset $E_{\Gamma,SiGeSn}-E_{\Gamma,GeSn}$ (meV)	Offset $E_{L,SiGeSn}-E_{\Gamma,GeSn}$ (meV)
DHS	447	83	191/98	119/99
MQW-A	509	32	79	45
MQW-B	529	8	71	22

Table 2 Bandgap, directness and conduction band offsets for the three investigated structures calculated at low temperatures. Quantization effects (energies of electron and hole ground states) are included in the "effective bandgap" values of MQW-A and MQW-B. The two values of offsets between the active area and claddings of DHS correspond to (i) the interface near the GeSn buffer and to (ii) the topmost barrier, which have different Sn and Si concentrations, see Table 1.

Photoluminescence (PL) spectra of all three as-grown structures are depicted in Figures 2a and 2b. At low temperatures, the emission intensity of MQW-A significantly outperforms the intensity of both, the DHS and MQW-B structures. The measured peak emission energies of 0.48 eV for DHS and 0.51 eV for MQW-A are in excellent agreement with the calculated effective bandgaps (see Table 2). Quantization effects are evidenced in the emission energy shift between MQW-A (0.51 eV) and B (0.53 eV). For MQW-B one can expect, that quantization will drastically reduce the directness of the GeSn well. This indeed results in a smaller carrier population in the Γ-valley and thus a weaker PL emission (cf. Figure 2a).

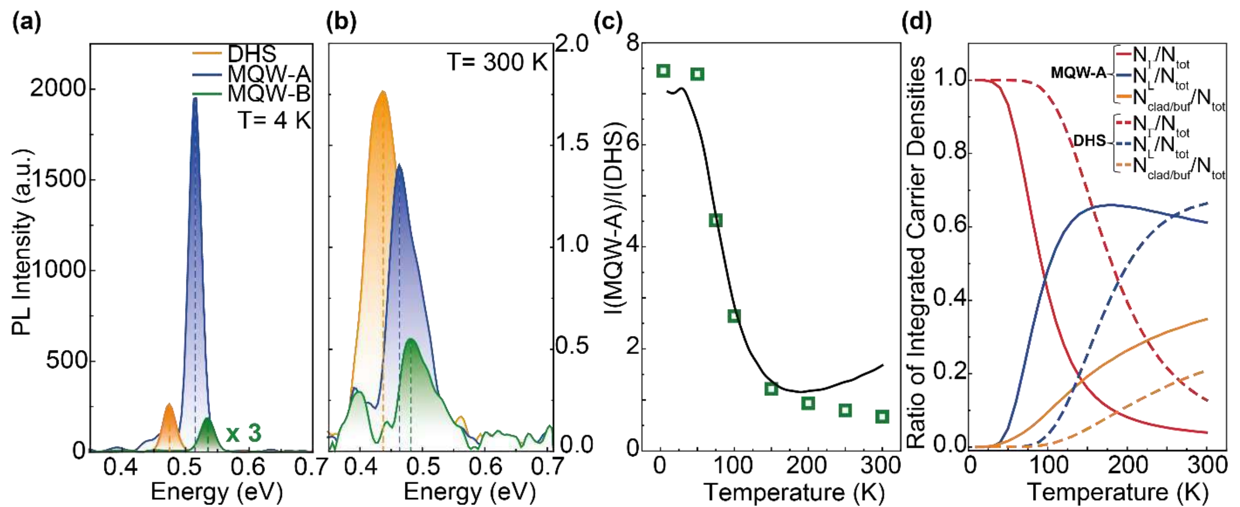

Figure 2 Photoluminescence of as-grown structures at **(a)** 4 K and **(b)** 300 K. At low temperature, the intensity for MQW-A (blue) is one order of magnitude higher compared to DHS (orange) and MQW-B

(green). **(c)** The ratio of integrated emission intensities from MQW-A and DHS vs. temperature (the experimental data and the calculated ratio respectively shown with green squares and black line). **(d)** Calculated electron fractional concentration (selectively integrated over respective layer thickness) of Γ- (red) and L-valleys (blue) in the active material, as well as in the barriers and $Ge_{0.9}Sn_{0.1}$ buffer layer (orange) for MQW-A (solid line) and DHS (dashed line).

The better performance of MQW-A, compared to DHS, with a PL enhancement by a factor of 7.45 at low temperatures, is attributed to a number of factors: (i) The modification of the joint density of states due to quantization improves the radiative recombination rates. This is a consequence of improved matching of in-plane heavy hole and Γ-electron effective masses, calculated to be $\sim$0.021 and $\sim$0.026 respectively[23]. We estimated the resulting improvement to be close to a factor of $\sim$2, which alone would be insufficient to fully explain the experimentally observed enhancement. (ii) An increase of non-radiative recombination times associated to the reduced number of bulk defects and/or the spatial separation of carriers from the misfit dislocations.

The temperature dependence of the PL ratio between MQW and DHS, shown in Figure 2c, comes from the decreased electron population of Γ (and increased population of the L- valleys) as the temperature rises. Since the L-valley population increases earlier in MQW-A than in DHS due to its reduced directness – a consequence of both, the lower Sn content and the quantization, as explained above – the PL enhancement is reduced as the measurement temperature increases. Additionally, at temperatures above ~50 K, the electrons increasingly escape from the wells of MQW-A into the barriers and underlying buffer, while for DHS delocalization from the active material only becomes significant above 100 K. The calculated relative electron population of Γ- and L- valleys in the gain material and of electrons inside the cladding/barrier/buffer, are given in Figure 2d. A more detailed description of the calculation of carrier concentrations can be found in the SI. In these calculations at 4 K, we assumed a carrier concentration of $\sim 4\cdot 10^{16}$ cm^{-3}, derived from the PL pumping with a 532 nm laser, averaged over the entire stack, cf. SI. The experimental data in Figure 2c is overlaid with a plot showing $(c_\Gamma \cdot c_{HH})_{MQW\text{-}A} / (c_\Gamma \cdot c_{HH})_{DHS}$ rescaled with an overall proportionality factor chosen to fit the experimental data, where c_Γ and c_{HH} are the Γ-electron and heavy hole concentrations in the MQW-A and DHS gain materials, respectively, taken from Figure 2d. The temperature dependence is well reproduced, pointing to the electron concentration – associated to the low barrier heights and low directness – as the limiting factor for the poor PL efficiency of the MQW-A sample at higher temperatures.

Microdisk Lasers

Microdisk laser cavities were fabricated from all three samples. A tilted scanning electron micrograph (SEM) of an MQW microdisk cavity with 8 µm diameter is shown in Figure 3a. The undercut geometry provides a high refractive index contrast between group IV materials and the surrounding air, which is very favorable in terms of increasing the mode overlap with the gain material as well as reducing bending losses. Additionally, the undercut leads to an elastic strain relaxation at the periphery of the microdisk and hence improves the directness of the gain material[24]. The strain distribution in such an under-etched disk, anchored by a thin pillar, is rather complex. The active material is not able to fully relax, since the relaxation is also constrained by the 200 nm $Ge_{0.9}Sn_{0.1}$ buffer and the SiGeSn barrier regions that have smaller lattice constants than the active regions. This is in contrast to the undercut single GeSn bulk films reported in Ref.[10], which were almost fully relaxed. Here, the microdisk bows slightly, similarly to a bimetal, with its rim moving downwards by (calculated) 43.1 nm relative to the center position. As a consequence, the strain also depends on the position of the quantum well along the z-direction (details are given in SI, Figure S2), with the top quantum well featuring a residual strain of -0.05%, which is significantly nearer to zero, i.e. to being a fully relaxed layer, than the -0.2% of the bottom quantum well. The simulated strain along the z-direction is shown in Figure 3b at the lateral position (x=0 µm, y=2.9 µm), indicated by the red point in the inset, which shows a schematic top view of a microdisk. This position is close to the outer rim and has a high overlap with the optical whispering gallery modes.

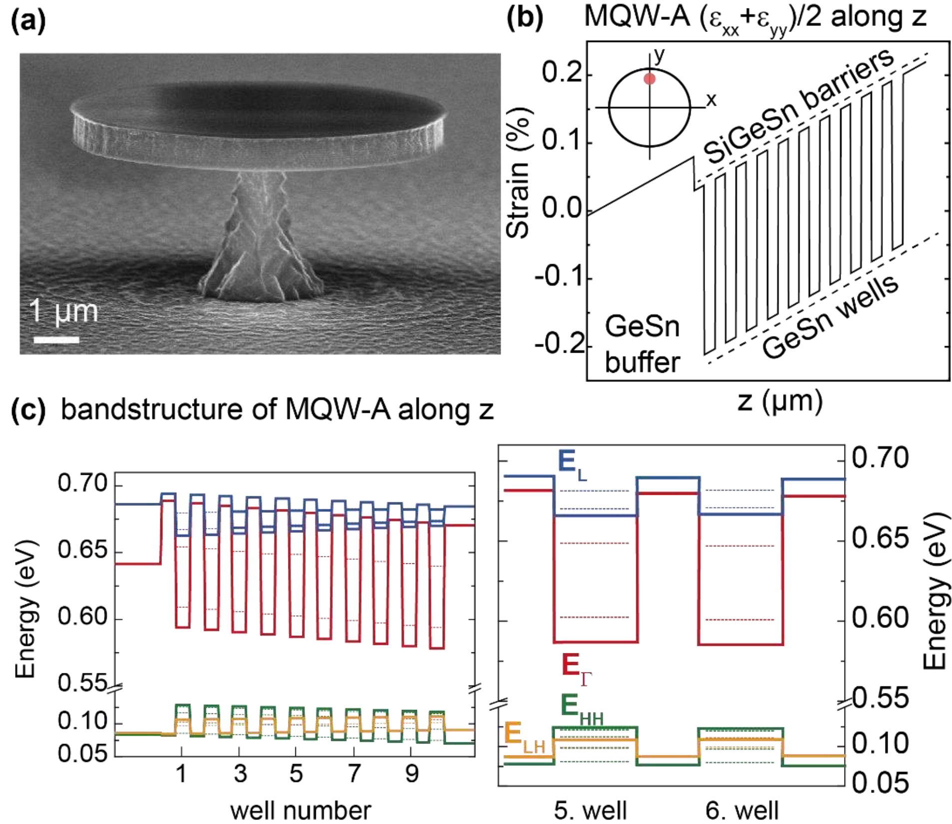

Figure 3 Microdisk design and strain analysis. **(a)** Tilted SEM of an MQW microdisk with 8 µm diameter and 3.5 µm undercut. **(b)** Modeled local strain along the z-direction at x=0 µm and y= 2.9 µm, i.e. at the red circle of the top-view microdisk in the inset, near the disk periphery, where the optical whispering gallery modes have large intensity. **(c)** Band diagram and confined states derived from the strain distribution from (b) for the whole stack (left) and two central QW's (right). Inside the wells, the bulk (solid) and quantized state energies (dotted lines) are shown for each of the valleys. Although, the biaxial symmetry is broken in the undercut disk geometry, notation as light and heavy hole bands is used. Light holes are attributed to lower (yellow) and heavy holes to the higher (dark green) effective mass in the direction perpendicular to the well plane, consistent with the quantization energies.

The corresponding band diagram along all 10 wells and along the two central wells of MQW-A is shown in Figure 3c. The quantized energy states in the wells are denoted by dotted lines. Compared to as-grown layers, due to strain relaxation the bandgaps are slightly red-shifted to values around 480 meV and the directness $\Delta E_{L-\Gamma}$ is increased from 32 meV to values between 58 meV and 79 meV, depending on the position of the well along the z-direction. After strain relaxation, the effective barrier height, defined previously as the energy difference between the lowest state in the well and the barrier conduction band

edge, is reduced to about 77 meV in all the QWs. We obtain 5 meV for the energy spread of the interband recombination energy, which is much less than the typically observed energy broadening of the PL and also smaller than the gain spectrum broadening associated to carrier scattering[25,26]. Therefore, we can assume that all quantum wells contribute to the gain during lasing operation.

Undercut microdisks were optically pumped under the conditions described in the method section. Since the emphasis in this work is on MQWs, the light-in light-out (L-L) characteristics of DHS and its temperature dependence are presented in SI, Figure S3. The threshold at 50 K is determined to be 250 kW/cm^2 and the maximum lasing temperature at 1064 nm pump wavelength is 120 K, similar to the values found for the corresponding bulk samples[10].

Figure 4 shows typical lasing characteristics of an MQW-A microdisk. Power dependent spectra of MQW-A, taken at 50 K with a spectral resolution of 16 cm^{-1} and pumping at 1064 nm, are presented in Figure 4a. At 72 kW/cm^2 peak pump power density, the dominant mode appears at an emission energy of 495 meV. A clear indication of lasing is given by the linewidth narrowing from 18 meV (at 27 kW/cm^2) down to 2.9 meV (at 125 kW/cm^2) shown in Figure 4b.

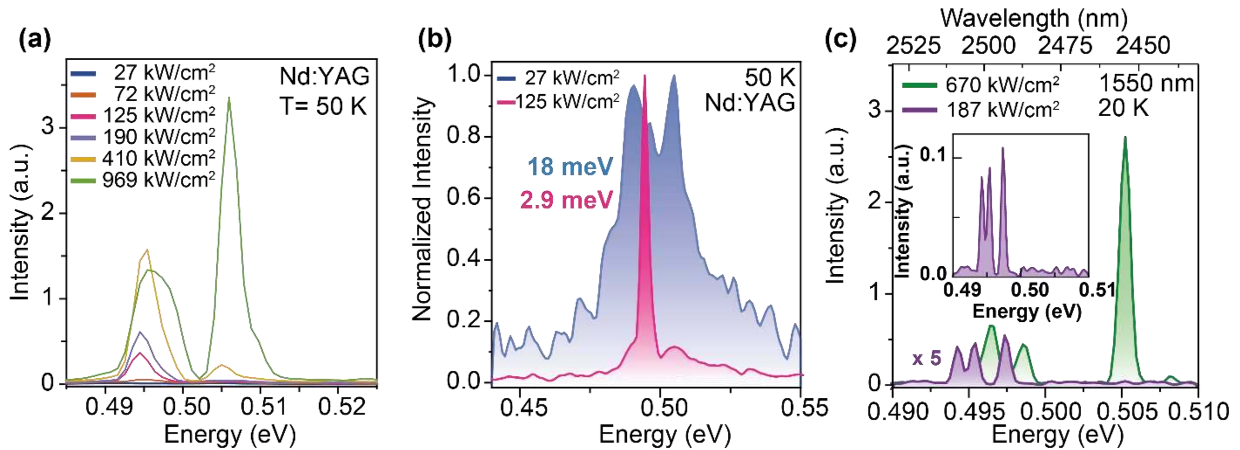

Figure 4 Laser performance of an 8 µm diameter MQW-A microdisk. **(a)** Lasing spectra at 50 K, taken with a 16 cm^{-1} resolution, for different Nd:YAG pumping powers. **(b)** Comparison of the emission spectra below and above threshold, where the expected linewidth narrowing is seen above threshold. **(c)** Lasing spectrum at 20 K, taken with a 4 cm^{-1} resolution and 1550 nm pumping, shows the linewidths between 0.65 (at 187 kW/cm^2) and 1 meV (at 670 kW/cm^2).

The lasing spectra taken with a resolution of 4 cm^{-1} (corresponding to 0.5 meV) taken at 20 K under 1550 nm optical pumping with a peak power density of 187 kW/cm^2 are shown in Figure 4c. The full width at half maximum (FWHM) of these spectra are between 0.65 meV and 1 meV, indicating that the

resolution in Figure 4b is not high enough to determine the exact linewidth. A detailed mode analysis shows that the three laser modes observed at 494 meV, 495 meV and 497 meV correspond to whispering gallery modes (WGM) with the same azimuthal mode number but different radial numbers, i.e. with different number of lobes along the radius of the microdisk. Once pumping levels exceed ~400 kW/cm^2, more modes at higher energies develop, cf. Figure 4a and c, and eventually become the dominant ones. The occurrence of higher order modes for MQW-A is accompanied by a higher overall slope efficiency, as shown in the 50 K L-L characteristic of Figure 5a. Similar effects were observed in the case of DHS microdisk. Based on the calculated group indices of the circularly travelling modes, the corresponding emission energy of 506 meV is consistent with an increase of the azimuthal mode number by one. The highest temperature at which laser emission occurred in MQW-A was 120 K, which is also shown in the temperature dependent emission spectra at a constant peak pump power density of 660 kW/cm^2 in Figure 5b.

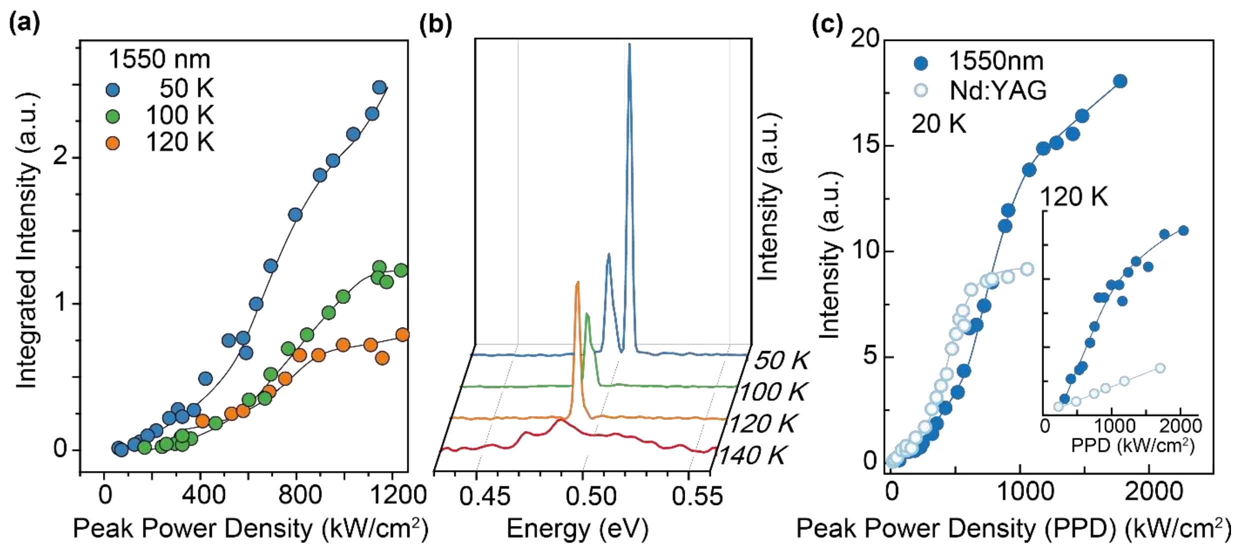

Figure 5 Lasing characteristics of MQW-A. **(a)** L-L curve of an 8 µm diameter disk from MQW-A under 1550 nm pumping. **(b)** Lasing spectra for 1550 nm pumping at different temperatures and with roughly the same pump intensity. At 140 K, the lasing action ceases and the spectrum reverts to the characteristic spectrum of spontaneous emission. **(c)** L-L curves for MQW-A for different laser excitation intensities at 20 K and 120 K (inset), showing large differences in output intensity.

The benefits of lower energy pumping are obvious in Figure 5c, comparing L-L curves for MQW-A pumped by the Nd:YAG laser, with photon energy of 1.16 eV, and by the 1550 nm laser (0.79 eV, but ~30% lower absorption than for the Nd:YAG laser). Two distinct features are apparent from measurements at 20 K: (i) Laser emission starts saturating at a much lower pump power density for the Nd:YAG laser than for the 1550 nm laser. This is ascribed to the higher excess photon energy – defined as the difference between

excitation and emission - of the Nd:YAG laser (0.66 eV) compared to the 1550 nm laser (0.30 eV) and the shorter pulse length. (ii) For the same reasons, the maximum lasing temperature is higher for pumping at 1550 nm (0.79 eV). At 120 K, the lasing has already ceased for Nd:YAG laser pumping, as seen by the completely linear L-L curve in Figure 5c inset, while it is still ongoing for 1550 nm pumping.

In order to compare the lasing thresholds in the MQW and the DHS samples, two methods to determine the threshold were used: from the PL peak emission at the lasing wavelength extracted from individual spectra, and also from the L-L curves obtained from the lock-in amplifier signals (i.e. resulting from integration over the full spectra). The threshold value is obtained from linear fit of these data sets in the region shortly after the lasing onset and finding the intercept with the abscissa (excitation power). All thresholds are shown as a peak power density, which contains an uncertainty due to the excitation spot size. A detailed discussion on spot size extraction is presented in S5. Additionally, in SI at 50 K and Nd:YAG pumping, a threshold value of (43 ± 7) kW/cm^2 is extracted for MWQ-A (Figure S4). This is close to the value found with the 1550 nm excitation. The lower pumping energy required with 1550 nm pump does not lead to a big difference in threshold values. It is used here to confirm the threshold behavior measured with the Nd:YAG excitation. The lowest threshold of (40± 5) kW/cm^2 was evaluated at a temperature of 20 K, as the average of thresholds for both lasers.

The clearly lower threshold of the MQW-A sample, compared to the DHS, is attributed to: (i) the reduction of the active volume[14], from 377 nm for the DHS active layer down to 220 nm for the cumulative well thicknesses in MQW-A, and (ii) a reduction of the density of states (DOS), contributing to a reduction of the transparency carrier concentration, and (iii) an increase in non-radiative lifetimes. Since the reduction of threshold is larger than the associated volume reduction (1.7 times), by an additional factor of 3.5, we tend to associate this additional factor to the DOS effect, reduced Auger and other non-radiative recombination processes due to quantization, dimensionality and confinement, as discussed in the analysis of the PL emission. To include these effects, as well as the dimensionality dependence of the dipole matrix elements, a detailed simulation analysis is required. But even without it, we can conclude that lifetime improvements due to localization of carriers in the present quantum wells are not yet as high as expected. Further pump probe experiments, such as the one reported in ref. [[27]], may help in clarifying that.

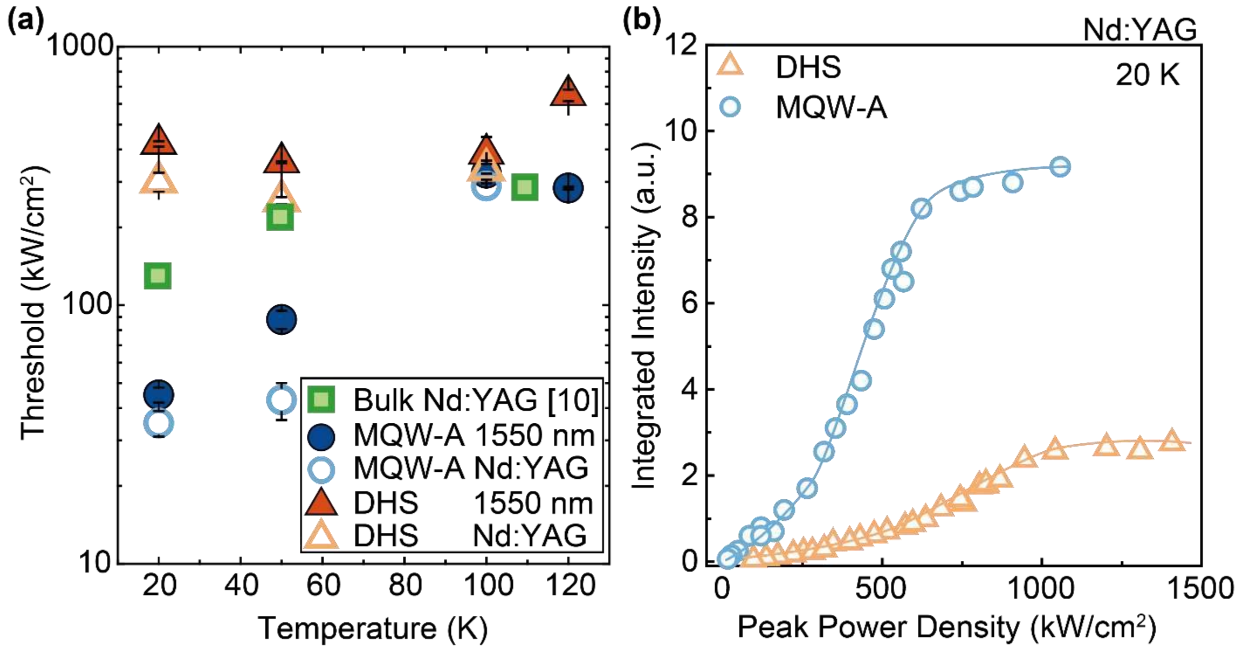

Figure 6 Comparison between the two types of laser pumping for different heterostructures. **(a)** Summary of threshold values of MQW-A (circles) and DHS (triangles) at different temperatures and pump laser type, shown in a semilogarithmic plot. Threshold values of the bulk MD with 12.5 at.% Sn from Ref. [10] are included in green. **(b)** 20 K integrated intensity versus peak power densities for MQW-A and DHS (Nd:YAG laser pumping).

The extracted threshold values for both DHS and MQW-A with both laser excitation sources are summarized in Figure 6a as a function of temperature. The values are obtained by the same method as described in Figure S3. Obviously, as discussed above, the MQW-A substantially outperforms the DHS at low temperatures and continues to outperform it up to temperatures of ~100 K. Once the temperature exceeds 100 K, due to (i) the relatively low energy separation $\Delta E_{L\text{-}\Gamma}$ and (ii) enhanced band filling because of reduced DOS increasing the electron quasi-Fermi level, both contributing to increased L-valley concentrations, the dimensionality advantages are lost. This is in line with the temperature dependence of the PL efficiency shown in Figure 2c. L-L-curves for both structures pumped with Nd:YAG are plotted in Figure 6b, showing that MQW-A outperforms DHS by a factor of 3 in emission power at low temperatures (20 K). Not that surprisingly, the sample with the higher PL efficiency (i.e. MQW-A) is also a more efficient laser emitter. A summary of maximal lasing temperatures and thresholds, for DHS and MQW-A under each pumping is provided in table 3.

Pumping wavelength (nm)	1550		1064	
Structure name	**Threshold at 20 K (kW/cm^2)**	**Max. lasing T (K)**	**Threshold at 20 K (kW/cm^2)**	**Max. lasing T (K)**
DHS	421 ± 10	120	300 ± 25	100
MQW-A	45 ± 3	120	35 ± 4	100

Table 3 Summary of threshold values at 20 K and maximal detected lasing temperature in MQW-A and DHS MDs for both pumping wavelengths.

Finally, we summarize the results for sample MQW-B. As explained above, quantization effects reduce the directness $\Delta E_{L-\Gamma}$ to 8 meV and thus strongly suppress lasing by increasing the threshold pump intensity. In fact, the strong quantization in wells may push the carriers into the buffer layer. Lasing spectra of microdisks with MQW-A and DHS are usually shifted to lower energies than PL peaks on blanket films because of strain relaxation. But this is actually not the case for MQW-B, where the low temperature PL emission of the blanket MQW-B is observed at 0.535 eV (cf. figure 2a), while the laser emission in microdisk occurs at 0.552 eV. Given that the bandgap of the $Ge_{0.9}Sn_{0.1}$ intermediate buffer layer is calculated to be 0.55 eV, it is likely that the observed lasing occurs in the GeSn buffer ($\Delta E_{L-\Gamma}$(blanket)= 57 meV) layer itself, rather than in the well region. The spectra at 20 K are depicted in Figure 7. Under Nd:YAG pumping, only spontaneous emission is observed under very high power densities, while pumping at 1550 nm shows signs of a lasing onset. Since the Nd:YAG pump is absorbed in the upper GeSn/SiGeSn MQW stack more than the 1550 nm pump, the output obtained with 1550 nm pump has >3 times larger intensity.

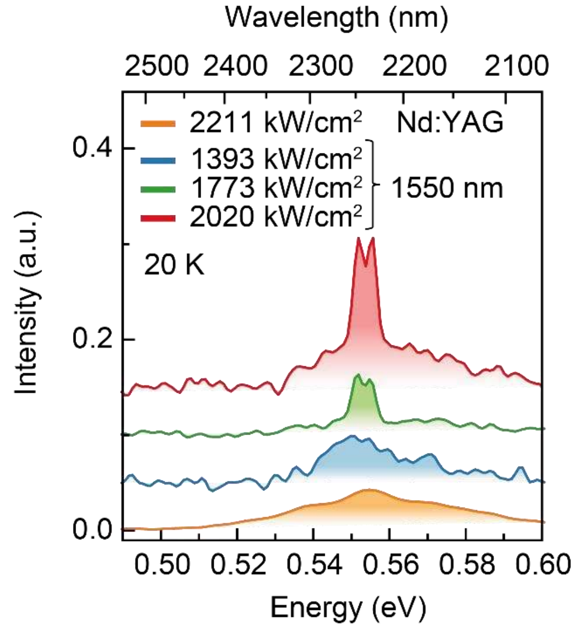

Figure 7 Spectra of MQW-B microdisk under optical pumping. For purpose of comparison, the intensities are normalized to duty cycles. Even for very strong 1550 nm pumping, laser emission can be hardly obtained. No lasing threshold has been reached with Nd:YAG pumping (in orange), only the spontaneous emission is observed.

We have investigated GeSn/SiGeSn multi quantum wells and heterostructures as laser material using the microdisk cavity geometry optically pumped with two pump photon energies. Theoretical predictions and experimental verification show reduced thresholds at low temperatures for the MQW-A design. This improvement, compared to the double heterostructures as well as to the previously investigated bulk systems, is attributed to: (i) reduced dimensionality, (ii) enhanced radiative recombination due to the localization of electrons and holes in quantum wells, (iii) spatial separation of lattice mismatch induced interface dislocations from the GeSn active medium by means of an intermediate buffer region, (iv) reduced non-radiative recombination rates associated to a reduced point defect density in the lower Sn content gain material (Sn (MQW) < Sn (DHS)). Furthermore, we observed limitations when decreasing quantum well thickness too much, because this leads to a considerable reduction of directness and thus of the material gain, as shown for MQW-B with 12 nm thick wells. The currently best performing structure, with a low threshold density of approximately 40 kW/cm^2, was the 10 periods MQW-A sample, which contains 22 nm thick barriers and 22 nm thick wells. To reach the longer-term goal of lasing at higher temperatures, one can consider a reduction of the number of wells, in order to achieve a uniform strain distribution, as well as using high potential barriers, with a higher Si content in the layers. Moreover,

strategies to reduce the point defects density, and thus the threshold density, will be necessary. Possible approaches include passivation[28] and/or high quality, lower Sn content GeSn materials in conjunction with tensile strain to boost the directness of GeSn[29].

METHODS

Epitaxial Growth

GeSn/SiGeSn heterostructures were grown by reactive gas source epitaxy in an industrial reduced-pressure chemical vapor deposition reactor[30]. Disilane (Si_2H_6), digermane (Ge_2H_6) and tin tetrachloride ($SnCl_4$) were used as precursors at growth temperatures between 350°C and 360°C. All heterostructures were grown on Ge buffered 200 mm industry grade Si(001) wafers[31]. A 200 nm thick, relaxed $Ge_{0.9}Sn_{0.1}$ layer was used as a buffer to accommodate the lattice mismatch between the Ge-VS and the GeSn/SiGeSn stacks on top. Residual compressive strain in the latter was thus minimized. The incorporation of Si inside the SiGeSn barriers is strongly dependent on the growth temperature, which is around 300°C for a $Ge_{0.87}Sn_{0.13}$ alloy. At these low temperatures, efficient cracking of the Disilane precursor becomes difficult, Ref. [20,32]. Hence, in the discussed heterostructures Si contents between 4.5 at.% and 5.5 at.% were reached.

Processing

Microdisk cavities were fabricated using conventional CMOS processing technology. A more detailed description of the used process can be found in Ref.[10]. It should be noted that, during the final underetching, only the underlying Ge-VS is removed, yielding suspended microdisks with the $Ge_{0.9}Sn_{0.1}$ buffer at the bottom (see Figure 3a).

Photoluminescence and Lasing Spectroscopy

Photoluminescence spectroscopy was performed on the three types of heterostructures using a chopped continuous wave laser emitting at 532 nm wavelength as excitation source. The collected emitted light was modulated in a Fourier-transform infrared (FTIR) spectrometer and detected by a liquid nitrogen cooled InSb detector. The GeSn/SiGeSn microdisks were investigated in an infrared microscope equipped with a 15x magnification objective of Schwarzschild type. Two laser sources coupled in a confocal fashion to the samples were used for optical excitation: either (i) a Nd:YAG (1064 nm) laser, with a pulse length of 5 ns and repetition rate of 17 kHz (corresponding to a duty cycle of $8.5\cdot10^{-5}$) or (ii) a fiber laser emitting at 1550 nm, with a pulse length of 800 ps and repetition rate of 20 kHz (duty cycle of $1.6\cdot10^{-5}$). The emission signal from the microdisks – collected via the same objective – was guided into an FTIR spectrometer and

measured by a similar liquid nitrogen cooled InSb detector. The excitation with 1550 nm laser is expected to be beneficial, because the photon energy is here nearer to the bandgap of the active GeSn material. This near-resonant excitation should reduce the heating of the generated carriers. However, the absorption at 1550 nm is estimated to be lower by about ~30% compared to the near infrared (1064 nm) case, after taking reflections at boundaries, absorption coefficients and thin film interference effects into account.

Modeling of strain distribution

The strain tensor of the undercut microdisks was modeled using the COMSOL Multiphysics programming package. The initial strain values of different layers in the as-grown samples – used in the modeling and experimentally measured by high resolution (HR)-XRD – are summarized in Table 4. Elastic coefficients are supposed to be those of Ge[33].

Structure	ε_{xx}	ε_{yy}	ε_{zz}
$Ge_{0.9}Sn_{0.1}$ buffer	$-0.38\cdot10^{-2}$	$-0.38\cdot10^{-2}$	$0.28\cdot10^{-2}$
$Ge_{0.867}Sn_{0.133}$ gain material	$-0.68\cdot10^{-2}$	$-0.68\cdot10^{-2}$	$0.51\cdot10^{-2}$
$Si_{0.048}Ge_{0.822}Sn_{0.13}$ barrier material	$-0.43\cdot10^{-2}$	$-0.43\cdot10^{-2}$	$0.32\cdot10^{-2}$

Table 4 Initial unprocessed film strain values prior to microdisk fabrication and undercutting. ε_{xx} and ε_{yy} have been measured by HR- XRD. ε_{zz} has been calculated based on the in-plane strain value and the elastic coefficients from Ref.[33].

Band structure calculations

Bandgaps in the relaxed alloys were calculated by quadratic interpolation with bowing parameters of $b_{GeSn,\Gamma}$ = 2.24 eV and $b_{SiSn,\Gamma}$ = 3.9 eV[34] at the Γ-point. The effective masses, necessary for calculation of quantized states, were derived using the 8-band k·p method and the effects of strain was included via deformation potentials[35]. The quantized states were calculated from the effective-mass Schrödinger equation, with the band discontinuities at interfaces given by the commonly used expressions[34], coming from the average valence band energy data of Jaros[36]. The bandgaps of GeSn active layers, the directness $\Delta E_{L-\Gamma}$ (defined as E_L-E_Γ) and the conduction band discontinuity between the active and barrier layers for DHS, MQW-A and MQW-B are listed in Table 2 for the as-grown stacks, hence without the elastic relaxation achieved by underetching of the microdisks. All calculations were performed for a low temperature of 4 K.

ACKNOWLEDGEMENTS

This work is supported by Deutsche Forschungsgemeinschaft (DFG) via the project "SiGeSn Laser for Silicon Photonics", and by The Royal Society International Exchange grant IE131593. The support of M. A. Schubert at IHP in the TEM measurements is gratefully acknowledged.

AUTHOR INFORMATION

J. M. H. fabricated the Ge-VS/Si substrates, N.v.d.D. and D.B. planned the (Si)GeSn epitaxial experiments and N.v.d.D. and D.R. grew the heterostructures. P.Z. and G.C. analyzed crystal quality via XRD, EDX and TEM analysis. D.R. and Z.I. did band structure calculations. Strain simulation was performed by B.M. and PL modeling by J.W.. D.S. carried out photoluminescence measurements of as-grown samples and fabricated microdisk cavities. D.S., T.Z. and F.A.P. measured optically pumped lasers. S.M., D.B., H.S., J.W. and D.G. supervised the experiments. D.S., D.B., J.W. and H.S. wrote the paper. All authors discussed the results and commented on the manuscript.

Conflict of Interests

The authors declare no conflict of interest.

ASSOCIATED CONTENT

Supporting Information. Additional information on the double heterostructure material and lasing performance, calculation of carrier densities and strain distribution, insight on the determination on thresholds and excitation spot size is given.

REFERENCES

(1) Rumley, S.; Bahadori, M.; Polster, R.; Hammond, S. D.; Calhoun, D. M.; Wen, K.; Rodrigues, A.; Bergman, K. Optical Interconnects for Extreme Scale Computing Systems. *Parallel Comput.* **2017**, *64*, 65–80.

(2) Lu, H.; Seabaugh, A. Tunnel Field-Effect Transistors: State-of-the-Art. *IEEE J. Electron Devices Soc.* **2014**, *2*, 44–49.

(3) Ionescu, A. M.; Riel, H. Tunnel Field-Effect Transistors as Energy-Efficient Electronic Switches. *Nature* **2011**, *479*, 329–337.

(4) Miller, D. A. B. Rationale and Challenges for Optical Interconnects to Electronic Chips. *Proc. IEEE*

2000, *88*, 728–749.

(5) Sun, C.; Wade, M. T.; Lee, Y.; Orcutt, J. S.; Alloatti, L.; Georgas, M. S.; Waterman, A. S.; Shainline, J. M.; Avizienis, R. R.; Lin, S.; Moss, B. R.; Kumar, R.; Pavanello, F.; Atabaki, A. H.; Cook, H. M.; Ou, A. J.; Leu, J. C.; Chen, Y.; Asanović, K.; Ram, R. J.; Popović, M. A.; Stojanović, V. M. Single-Chip Microprocessor That Communicates Directly Using Light. *Nature* **2015**, *528*, 534–538.

(6) Kryzhanovskaya, N.; Moiseev, E.; Polubavkina, Y.; Maximov, M.; Kulagina, M.; Troshkov, S.; Zadiranov, Y.; Guseva, Y.; Lipovskii, A.; Tang, M.; Liao, M.; Wu, J.; Chen, S.; Liu, H.; Zhukov, A. Heat-Sink Free CW Operation of Injection Microdisk Lasers Grown on Si Substrate with Emission Wavelength beyond 13 Mm. *Opt. Lett.* **2017**, *42*, 3319.

(7) Wan, Y.; Jung, D.; Norman, J.; Shang, C.; MacFarlane, I.; Li, Q.; Kennedy, M. J.; Gossard, A. C.; Lau, K. M.; Bowers, J. E. O-Band Electrically Injected Quantum Dot Micro-Ring Lasers on on-Axis (001) GaP/Si and V-Groove Si. *Opt. Express* **2017**, *25*, 26853.

(8) Krishnamoorthy, A. V.; Goossen, K. W.; Jan, W.; Zheng, X.; Ho, R.; Li, G.; Rozier, R.; Liu, F.; Patil, D.; Lexau, J.; Schwetman, H.; Feng, D.; Asghari, M.; Pinguet, T.; Cunningham, J. E. Progress in Low-Power Switched Optical Interconnects. *IEEE J. Sel. Top. Quantum Electron.* **2011**, *17*, 357–376.

(9) Wirths, S.; Geiger, R.; von den Driesch, N.; Mussler, G.; Stoica, T.; Mantl, S.; Ikonic, Z.; Luysberg, M.; Chiussi, S.; Hartmann, J. M.; Sigg, H.; Faist, J.; Buca, D.; Grützmacher, D. Lasing in Direct-Bandgap GeSn Alloy Grown on Si. *Nat. Photonics* **2015**, *9*, 88–92.

(10) Stange, D.; Wirths, S.; Geiger, R.; Schulte-Braucks, C.; Marzban, B.; Driesch, N. von den; Mussler, G.; Zabel, T.; Stoica, T.; Hartmann, J.-M.; Mantl, S.; Ikonic, Z.; Grützmacher, D.; Sigg, H.; Witzens, J.; Buca, D. Optically Pumped GeSn Microdisk Lasers on Si. *ACS Photonics* **2016**, *3*, 1279–1285.

(11) Al-Kabi, S.; Ghetmiri, S. A.; Margetis, J.; Pham, T.; Zhou, Y.; Dou, W.; Collier, B.; Quinde, R.; Du, W.; Mosleh, A.; Liu, J.; Sun, G.; Soref, R. A.; Tolle, J.; Li, B.; Mortazavi, M.; Naseem, H. A.; Yu, S. An Optically Pumped 2.5µm GeSn Laser on Si Operating at 110 K. *Appl. Phys. Lett.* **2016**, *109*, 171105.

(12) Margetis, J.; Al-Kabi, S.; Du, W.; Dou, W.; Zhou, Y.; Pham, T.; Grant, P.; Ghetmiri, S.; Mosleh, A.; Li, B.; Liu, J.; Sun, G.; Soref, R.; Tolle, J.; Mortazavi, M.; Yu, S.-Q. Si-Based GeSn Lasers with Wavelength Coverage of 2-3 µm and Operating Temperatures up to 180 K. *ACS Photonics* **2018**, *5*, 827–833.

(13) Reboud, V.; Gassenq, A.; Pauc, N.; Aubin, J.; Milord, L.; Thai, Q. M.; Bertrand, M.; Guilloy, K.;

Rouchon, D.; Rothman, J.; Zabel, T.; Armand Pilon, F.; Sigg, H.; Chelnokov, A.; Hartmann, J. M.; Calvo, V. Optically Pumped GeSn Micro-Disks with 16% Sn Lasing at 3.1µm up to 180 K. *Appl. Phys. Lett.* **2017**, *111*, 092101.

(14) Arakawa, Y.; Yariv, A. Quantum Well Lasers--Gain, Spectra, Dynamics. *IEEE J. Quantum Electron.* **1986**, *22*, 1887–1899.

(15) Sun, G.; Soref, R. A.; Cheng, H. H. Design of a Si-Based Lattice-Matched Room-Temperature GeSn/GeSiSn Multi-Quantum-Well Mid-Infrared Laser Diode. *Opt. Express* **2010**, *18*, 19957.

(16) Agrawal, G. P.; Dutta, N. K. *Semiconductor Lasers*; 1993.

(17) Stange, D.; von den Driesch, N.; Rainko, D.; Schulte-Braucks, C.; Wirths, S.; Mussler, G.; Tiedemann, A. T.; Stoica, T.; Hartmann, J. M.; Ikonic, Z.; Mantl, S.; Grützmacher, D.; Buca, D. Study of GeSn Based Heterostructures: Towards Optimized Group IV MQW LEDs. *Opt. Express* **2016**, *24*, 1358.

(18) Stange, D.; von den Driesch, N.; Rainko, D.; Roesgaard, S.; Povstugar, I.; Hartmann, J.-M.; Stoica, T.; Ikonic, Z.; Mantl, S.; Grützmacher, D.; Buca, D. Short-Wave Infrared LEDs from GeSn/SiGeSn Multiple Quantum Wells. *Optica* **2017**, *4*, 185.

(19) Du, W.; Ghetmiri, S. A.; Margetis, J.; Al-Kabi, S.; Zhou, Y.; Liu, J.; Sun, G.; Soref, R. A.; Tolle, J.; Li, B.; Mortazavi, M.; Yu, S.-Q. Investigation of Optical Transitions in a SiGeSn/GeSn/SiGeSn Single Quantum Well Structure. *J. Appl. Phys.* **2017**, *122*, 123102.

(20) von den Driesch, N.; Stange, D.; Rainko, D.; Povstugar, I.; Zaumseil, P.; Capellini, G.; Schröder, T.; Denneulin, T.; Ikonic, Z.; Hartmann, J.-M.; Sigg, H.; Mantl, S.; Grützmacher, D.; Buca, D. Advanced GeSn/SiGeSn Group IV Heterostructure Lasers. *Adv. Sci.* **2018**, *5*, 1700955.

(21) Wang, W.; Zhou, Q.; Dong, Y.; Tok, E. S.; Yeo, Y.-C. Critical Thickness for Strain Relaxation of $Ge_{1-x}Sn_x$ ($X \leq 0.17$) Grown by Molecular Beam Epitaxy on Ge(001). *Appl. Phys. Lett.* **2015**, *106*, 232106.

(22) Lu Low, K.; Yang, Y.; Han, G.; Fan, W.; Yeo, Y.-C. Electronic Band Structure and Effective Mass Parameters of Ge1−xSnx Alloys. *J. Appl. Phys.* **2012**, *112*, 103715.

(23) Yablonovitch, E.; Kane, E. Reduction of Lasing Threshold Current Density by the Lowering of Valence Band Effective Mass. *J. Light. Technol.* **1986**, *4*, 504–506.

(24) Gupta, S.; Chen, R.; Huang, Y. C.; Kim, Y.; Sanchez, E.; Harris, J. S.; Saraswat, K. C. Highly Selective

Dry Etching of Germanium over Germanium-Tin $Ge_{1-x}Sn_x$: A Novel Route for $Ge_{1-x}Sn_x$ Nanostructure Fabrication. *Nano Lett.* **2013**, *13*, 3783–3790.

(25) Nagarajan, R.; Kamiya, T.; Kurobe, A. Band Filling in GaAs/AlGaAs Multiquantum Well Lasers and Its Effect on the Threshold Current. *IEEE J. Quantum Electron.* **1989**, *25*, 1161–1170.

(26) Prost, M.; El Kurdi, M.; Aniel, F.; Zerounian, N.; Sauvage, S.; Checoury, X.; Bœuf, F.; Boucaud, P. Analysis of Optical Gain Threshold in N-Doped and Tensile-Strained Germanium Heterostructure Diodes. *J. Appl. Phys.* **2015**, *118*.

(27) Geiger, R. Direct Band Gap Germanium for Si-compatible Lasing, ETH Zurich, 2016.

(28) Jung, W.; Park, J.; Nainani, A.; Nam, D.; Saraswat, K. C. Fluorine Passivation of Vacancy Defects in Bulk Germanium for Ge Metal-Oxide-Semiconductor Field-Effect Transistor Application. *Appl. Phys. Lett.* **2012**, *101*, 072104.

(29) Millar, R. W.; Dumas, D. C. S.; Gallacher, K. F.; Jahandar, P.; MacGregor, C.; Myronov, M.; Paul, D. J. Mid-Infrared Light Emission >3µm Wavelength from Tensile Strained GeSn Microdisks. *Opt. Express* **2017**, *25*, 25374.

(30) von den Driesch, N.; Stange, D.; Wirths, S.; Mussler, G.; Holländer, B.; Ikonic, Z.; Hartmann, J. M.; Stoica, T.; Mantl, S.; Grützmacher, D.; Buca, D. Direct Bandgap Group IV Epitaxy on Si for Laser Applications. *Chem. Mater.* **2015**, *27*, 4693–4702.

(31) Hartmann, J. M.; Abbadie, A.; Cherkashin, N.; Grampeix, H.; Clavelier, L. Epitaxial Growth of Ge Thick Layers on Nominal and 6° off Si(001); Ge Surface Passivation by Si. *Semicond. Sci. Technol.* **2009**, *24*, 055002.

(32) von den Driesch, N.; Stange, D.; Wirths, S.; Rainko, D.; Povstugar, I.; Savenko, A.; Breuer, U.; Geiger, R.; Sigg, H.; Ikonic, Z.; Hartmann, J.; Grützmacher, D.; Mantl, S.; Buca, D. SiGeSn Ternaries for Efficient Group IV Heterostructure Light Emitters. *Small* **2017**, *13*, 1603321.

(33) Fine, M. E. Elastic Constants of Germanium between 1.7° and 80°K. *J. Appl. Phys.* **1955**, *26*, 862–863.

(34) Moontragoon, P.; Soref, R. A.; Ikonić, Z. The Direct and Indirect Bandgaps of Unstrained $Si_xGe_{1-x-y}Sn_y$ and Their Photonic Device Applications. *J. Appl. Phys.* **2012**, *112*, 073106.

(35) Bahder, T. B. Erratum: Eight-Band kp Model of Strained Zinc-Blende Crystals [Phys. Rev. B 41, 11

992 (1990)]. *Phys. Rev. B* **1992**, *46*, 9913–9913.

(36) Jaros, M. Simple Analytic Model for Heterojunction Band Offsets. *Phys. Rev. B* **1988**, *37*, 7112–7114.

Supplementary Information:

GeSn/SiGeSn Heterostructure and Multi Quantum Well Lasers

Daniela Stange[1*], Nils von den Driesch[1,2], Thomas Zabel[3], Francesco Armand-Pilon[3], Denis Rainko[1], Bahareh Marzban[4], Peter Zaumseil[5], Jean-Michel Hartmann[6], Zoran Ikonic[7], Giovanni Capellini[5,8], Siegfried Mantl[1], Hans Sigg[3], Jeremy Witzens[4], Detlev Grützmacher[1], and Dan Buca[1]

[1]Peter Grünberg Institute (PGI 9) and JARA-Fundamentals of Future Information Technologies, Forschungszentrum Jülich, 52425 Jülich, Germany

[2]JARA-Institute Green IT, RWTH Aachen University, 52075 Aachen, Germany

[3]Laboratory for Micro- and Nanotechnology (LMN), Paul Scherrer Institute, CH-5232 Villigen, Switzerland

[4]Institute of Integrated Photonics and JARA-Fundamentals of Future Information Technologies, RWTH Aachen University, 52074 Aachen, Germany

[5]IHP, Im Technologiepark 25, 15236 Frankfurt (Oder), Germany

[6]Univ. Grenoble Alpes, CEA, LETI, F-38000 Grenoble, France

[7]Pollard Institute, School of Electronic and Electrical Engineering, University of Leeds, Leeds LS2 9JT, United Kingdom

[8]Department of Sciences, Università Roma Tre, 00146 Roma, Italy

This file contains: 7 pages, 5 figures

Double Heterostructure- Material S24

Carrier density calculation..S24

Strain simulation S25

Double Heterostructure- Lasing S26

Threshold determinations...S28

Laser spot size determination S28

Double Heterostructure- Material

A cross-section transmission electron micrograph (X-TEM) of the DHS comprising a 380 nm thick $Ge_{0.855}Sn_{0.145}$ active region sandwiched between 50 nm thick SiGeSn cladding layers is shown in Figure SI1. The double heterostructure incorporates GeSn with a higher Sn concentration as the GeSn buffer, on top of which it is grown. Therefore, a large strain builds up inside the heterostructure and the heterostructure unintentionally relaxes further after the critical thickness is exceeded. The misfit dislocations formed when relaxation takes place are located at the interface between the SiGeSn cladding and the GeSn active layer, which is detrimental for radiative recombination efficiency.

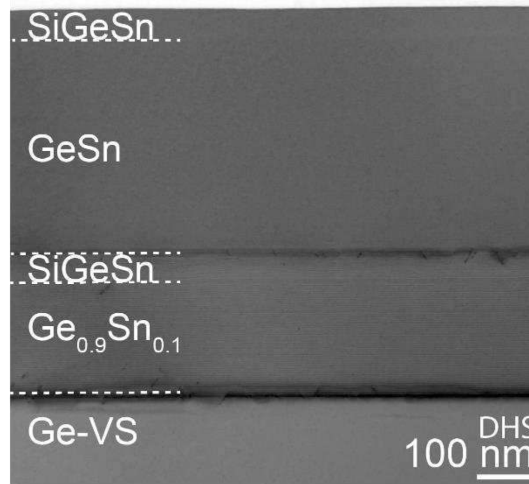

Figure S1 A TEM of the DHS structure reveals misfit dislocation at the interface between the SiGeSn bottom cladding and the active GeSn layer, which are generated by further strain relaxation of the heterostructure stack.

Carrier density calculation

The ratio of the carrier densities, discussed in Figure 2d of the main text, is evaluated as follows. For both layer stacks, a constant excitation power density of 3.4 kW/cm^2 is assumed for the 532 nm laser wavelength. This results in an average carrier density of ~$4{\cdot}10^{16}$ cm^{-3} inside the MQW and DHS epitaxial stacks, assuming recombination rates to be dominated by non-radiative recombination with a carrier lifetime of ~300 ps (and almost equal total stack thicknesses). Carrier concentrations are expected to be low enough for screening/band-bending effects to be neglected, i.e. the flat band condition is assumed. In addition, carriers are supposed to be at thermal equilibrium, with the associated electron and hole quasi-Fermi-levels $E_{fc,v}$, so that carrier concentrations averaged over the entire stacks are simply given by

$$n = \frac{1}{w} \sum_{\Gamma,L\ /\ HH,LH} \int \frac{\rho_{c,v}(E)dE}{1 + \exp[\pm \frac{E - E_{fc,v}}{k_B T}]}$$

and are equal for electrons and holes due to overall charge neutrality. Here, w is the total stack thickness, $\rho_{c,v}(E)$ is the local density of states for the conduction or valence bands in a given layer, k_B Boltzmann's constant and T the temperature. The integral is taken over the entire stack and the summation over all the relevant valleys, Γ, L for electrons and HH, LH for holes. In the first step, the quasi-Fermi-levels required to obtain the targeted average concentration are iteratively determined. In the second step, the carrier concentrations are determined in each of the valleys inside the active material. By repeating the calculation at different temperatures, the data required to generate the modeling curve in Figure 2d was obtained. As a final remark it should be noted that the relevant assumptions are the flat-band condition, carrier concentrations according to thermodynamic equilibrium relative to the quasi-Fermi levels, equal excitation densities and recombination rates dominated by similar dark recombination rates – the specific carrier concentrations in the above are only given to exemplify orders of magnitude.

Strain simulation

The calculated strain in the radial plane of the MQW-A microdisk is plotted in Figure SI2 for two different wells. The top well (orange) exhibits a higher degree of relaxation than the bottom well (blue), i.e. -0.05% vs. -0.2% residual compressive strain. This is due to elastic bending of the disk, stretching the top well more than the bottom well. In contrast to that, the regions directly above the pillar show a different behavior due to anchoring. The strongly varying strain values at the edges of the disk are calculation artefacts without any physical meaning.

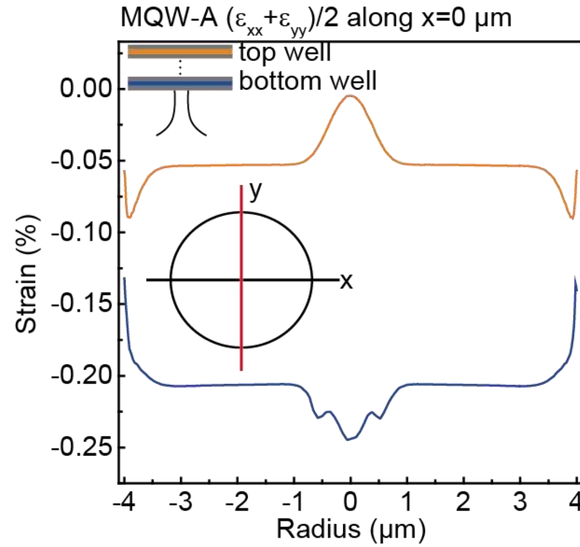

Figure S2 Distribution of $(\varepsilon_{xx}+\varepsilon_{yy})/2$ strain component, along y (x=0) in the bottom and top wells of MQW-A microdisk. The red line shows the direction along which the strain was calculated.

Double Heterostructure- Lasing

The performance of a 8 µm diameter DHS microdisk laser, pumped at 1064 nm (Nd:YAG laser), is shown in Figure SI3. Lasing spectra taken at 20 K for different pump powers demonstrate the transitions from spontaneous emission to lasing and finally to spectrally multimode operation. The light-in light-out (L-L) characteristics are presented for three different temperatures in Figure SI4b. As shown previously[11,12,25], the slope efficiency of the GeSn laser sharply decreases as the temperature increases. For DHS, the threshold at 50 K is determined to be 250 kW/cm^2, which can also be seen in the emission spectrum collapse in Figure 4a. At about ~700 kW/cm^2, the slope efficiency of the L-L curve at 50 K markedly increases. This regime coincides with the onset of multi-mode operation in Figure 4a. At ~1000 kW/cm^2 the laser output power saturates due to thermal and band filling effects. In comparison to the bulk GeSn based laser structures reported earlier[14,25], the introduction of SiGeSn claddings does not appear to improve the lasing threshold excitation density. This undesirable result is partially ascribed to the fact that the (still existing) defective interface between the lower SiGeSn barrier and the active material, to which carriers inside the well are directly exposed, continues to contribute to non-radiative carrier recombination (NRCR). The generally higher threshold values reported for higher Sn content lasers in Ref.[25] and Ref.[14] indicate that the defect densities likely increase for increasing Sn concentrations. The L-L temperature characteristics for DHS shown in Figure SI4b indicate that the lasing ceases at a temperature of 120 K, since the linearity of the L-L curve throughout the whole range of pumping levels implies a spontaneous emission dominated luminescence. In line with threshold density values, the

maximum lasing temperature has not essentially improved in this heterostructure. These results suggest that other improvements paths such as 2D heterostructures have to be explored on the way towards more efficient lasing.

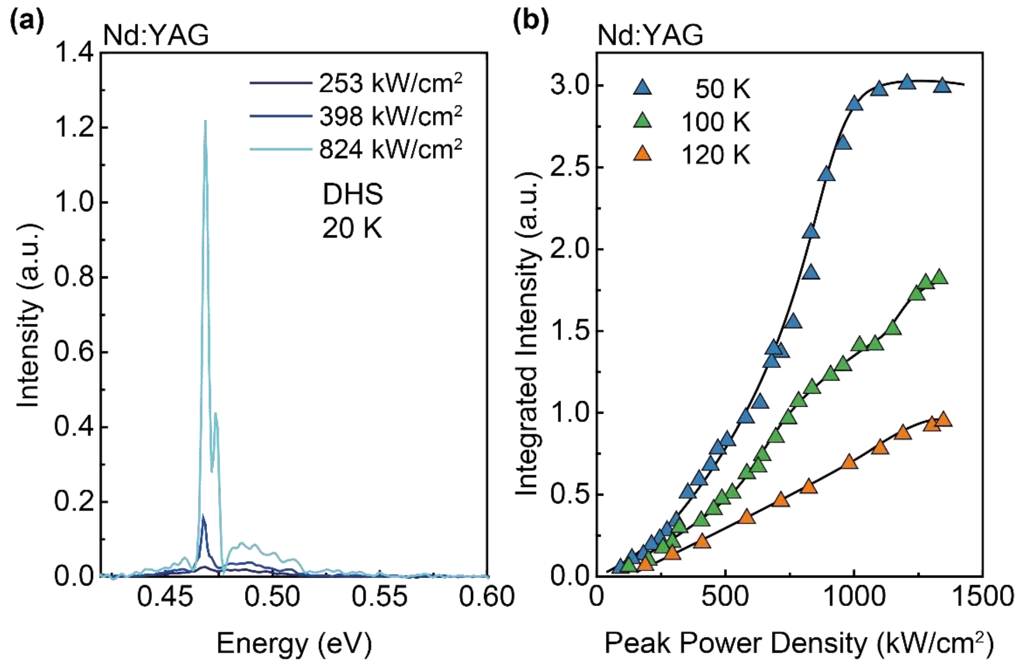

Figure S3 Emission characteristics of a DHS microdisk (8 µm diameter). **(a)** Spectra for increasing pumping powers showing spontaneous emission lasing near threshold and multimode lasing at high pump power, respectively. **(b)** Light-in light-out curves taken at three different temperatures. The Nd:YAG laser pumping was used for (a) and (b).

Threshold determinations

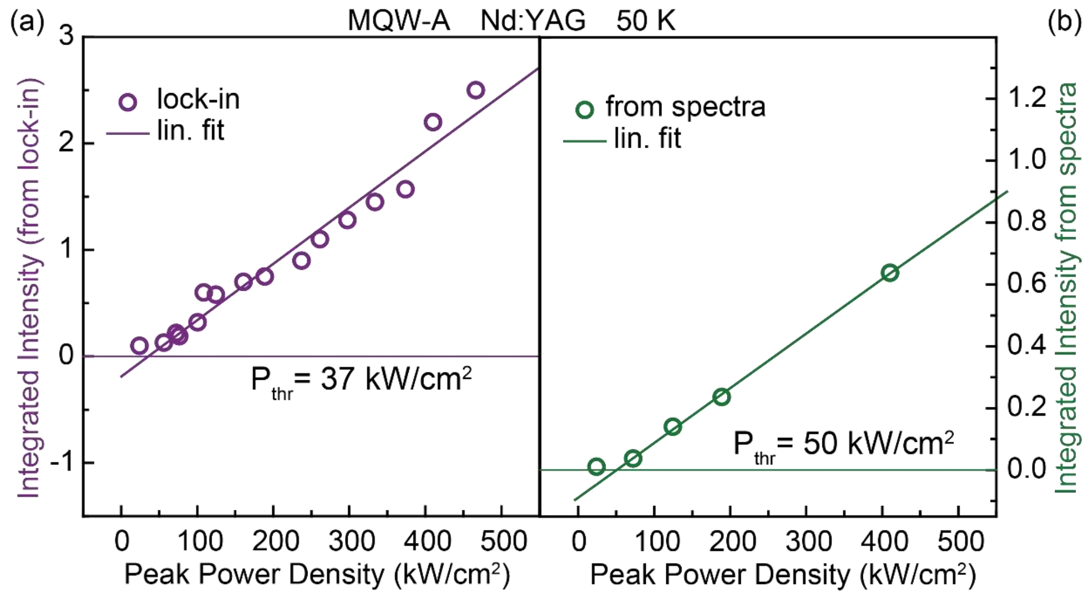

Figure S4 Linear fit for threshold determination from two different data sets: the integrated emission intensity obtained by the lock-in amplifier (in (a) purple) and obtained from the recorded spectra (in (b) green), both measured at 50 K with Nd:YAG pumping.

A straight line is fitted to (i) values obtained directly by the lock-in amplifier (purple data points, Figure SI4a) and (ii) the emission intensity obtained from the integration of individual spectra (green data points, Figure SI4b) at the same temperature and for the same device at pumping powers around the lasing onset. The threshold value is determined by the intersection of the fit with the abscissa. The average of both values is given in the manuscript as threshold while their difference is given as the measurement uncertainty. Combining both, a lasing threshold of (43 ± 7) kW/cm^2 peak power density at 50 K is extracted.

Laser spot size determination

The laser spot size of the excitation lasers is used to determine the peak power densities used in the manuscript. Therefore, the error on this determination influences the extracted threshold values. In the following the determination procedure is described.

The laser power is measured with a power meter close to the sample position, while a razorblade is driven through the laser spot at the sample position with a resolution of 1 µm steps. The resulting intensity profile is plotted in figure SI5a.

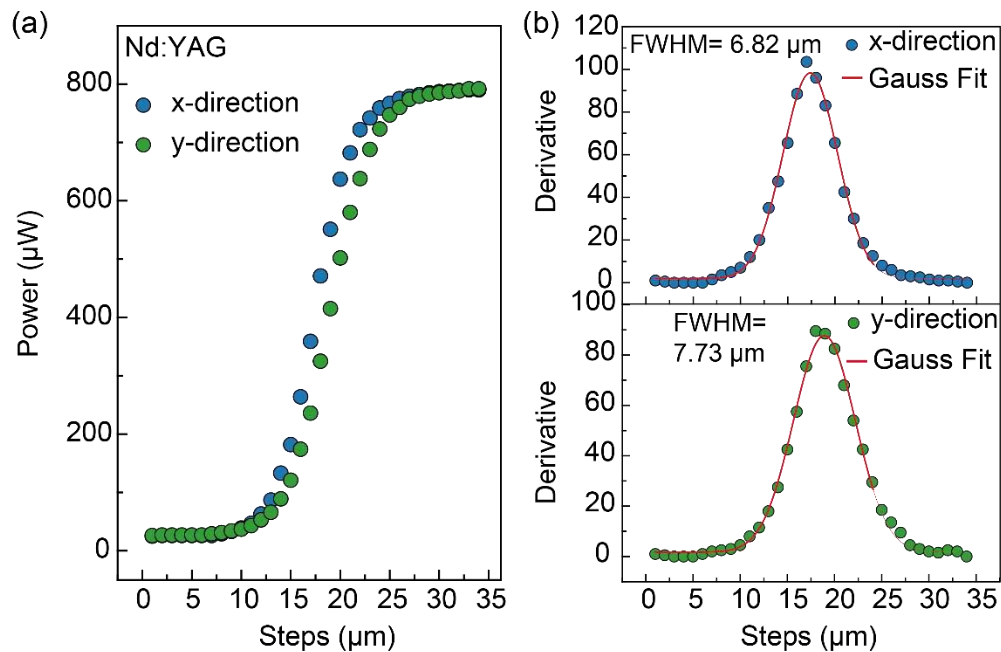

Figure S5 Intensity profile of the excitation spot of the Nd:YAG laser in the horizontal and vertical directions (a). The derivative of this profile shows a Gaussian beam (b).

With the derivative of this data, the Gaussian beam profile can be fitted in the x- (horizontal) as well as in the y-direction (vertical). The beam size is determined as the FWHM of the Gauss function and the mean value of the x- and y- directions is taken as spot diameter, assuming a circular excitation spot geometry. In the case of Nd:YAG excitation, the spot diameter is determined to be (7.3±0.2) µm, while the spot size for excitation with 1550 nm is determined in the same manner and results in (6.9±0.7) µm.